INTERFACE SCIENCE 10, 121–136, 2002

Linking Phase-Field and Atomistic Simulations to Model Dendritic Solidification in Highly Undercooled Melts

JEAN BRAGARD, ALAIN KARMA AND YOUNGYIH H. LEE*
Department of Physics and Center for Interdisciplinary Research on Complex Systems, Northeastern University, Boston, MA 02115, USA

MATHIS PLAPP
Laboratoire de Physique de la Matière Condensée, CNRS/Ecole Polytechnique, 91128 Palaiseau, France

Abstract. Even though our theoretical understanding of dendritic solidification is relatively well developed, our current ability to model this process quantitatively remains extremely limited. This is due to the fact that the morphological development of dendrites depends sensitively on the degree of anisotropy of capillary and/or kinetic properties of the solid-liquid interface, which is not precisely known for materials of metallurgical interest. Here we simulate the crystallization of highly undercooled nickel melts using a computationally efficient phase-field model together with anisotropic properties recently predicted by molecular dynamics simulations. The results are compared to experimental data and to the predictions of a linearized solvability theory that includes both capillary and kinetic effects at the interface.

Keywords: solidification, phase-field, dendrites, crystalline anisotropy, interface kinetics, metallic melts

1. Introduction and Overview

The freezing of a supercooled liquid or a supersaturated liquid mixture of two or more components generally leads to the formation of highly branched dendritic crystals in materials where the solid-liquid interface is rough on an atomic scale, but smooth on a macroscopic scale [1]. This process is of considerable practical importance to metallurgists because commercial metallic alloys often form dendrites during freezing, and the resulting microstructure controls the properties of the final solidification product [2]. Moreover, dendritic growth has been of fundamental interest to physicists in the general context of pattern formation in non-equilibrium dissipative systems [3–5].

The solidification of a pure undercooled melt is one of the simplest methods to form dendritic crystals and to investigate their growth behavior and morphology under well-controlled conditions. For this reason, this process has been extensively studied both theoretically and experimentally for several decades. Traditionally, experimental studies have focused on the characterization of the unique relationship between the steady-state growth velocity V of the dendrite tip and the bulk undercooling $\Delta T = T_M - T_\infty$, where T_M is the melting point temperature and T_∞ is the initial temperature of the melt.

A first major step in the development of the theory of dendritic growth was made over half a century ago by Ivantsov [6] who analyzed this problem in the simplifying limit where both capillary and kinetic effects at the interface are neglected. In this approximation, the solid-liquid interface grows at the melting temperature and the only rate-limiting process is the diffusive transport of the latent heat of freezing into the undercooled liquid. The basic equations governing the growth are then the diffusion

*Present address: Department of Radiation Oncology, Yonsei University, College of Medicine, Seoul 132, Korea.

equation

$$\frac{\partial T}{\partial t} = D\nabla^2 T, \tag{1}$$

and the condition of heat conservation at the growing interface

$$LV_n = c_p D\hat{n} \cdot (\vec{\nabla} T|_S - \vec{\nabla} T|_L), \tag{2}$$

where V_n is the normal velocity of the interface, $\hat{n}$ is the directional normal to the interface pointing into the liquid and $\hat{n} \cdot \vec{\nabla} T|_{S,L}$ is the normal gradient of temperature on the solid (S) or liquid (L) side of the interface; also, L and c_p are, respectively, the latent heat of freezing and the specific heat at constant pressure per unit volume, and D is the thermal diffusivity (with both c_p and D taken here to be the same in both phases).

Ivantsov looked for needle-shape steady-state solutions of Eqs. (1) and (2) growing at a constant velocity V. The assumption that growth takes place in steady-state allows one to replace $\partial T/\partial t$ in Eq. (1) by $-V\partial T/\partial z$ in a frame of reference moving with respect to the sample at speed V, where $+z$ is the growth direction. The constraint that the needle shape is preserved in time implies that $V_n = V\cos\theta$, where θ is the angle between $\hat{n}$ and the z-axis. Remarkably, Ivantsov found that paraboloids of revolution are exact solutions to this steady-state growth problem for an isothermal interface at $T = T_M$. Moreover, he derived a relationship between the Péclet number, $P = \rho V/(2D)$, where ρ is the dendrite tip radius, and the dimensionless undercooling $\Delta T/(L/c_p)$. Three decades later, Glicksman et al. [7] demonstrated by accurate measurements in a transparent organic system that this relation is well satisfied.

The Ivantsov relation does not predict V and ρ independently, but only their product. Consequently, theoretical studies subsequent to Ivantsov's work concentrated on understanding how this velocity is uniquely determined by including capillary and kinetic effects. These effects make the interface non-isothermal, with a temperature determined by the classic Gibbs-Thomson condition augmented to allow for a departure from local equilibrium

$$T_I = T_M - \frac{T_M}{L}\sum_{i=1,2}\left[\gamma(\hat{n}) + \frac{\partial^2\gamma(\hat{n})}{\partial\theta_i^2}\right]\frac{1}{R_i} - \frac{V_n}{\mu(\hat{n})}. \tag{3}$$

The second term on the right-hand-side of Eq. (3) represents the purely equilibrium effect of capillary forces on the temperature of a curved interface, where $\gamma(\hat{n})$ is the excess free-energy of the solid-liquid interface, θ_i are the local angles between the normal direction $\hat{n}$ and the two local principal directions on the interface, and R_i are the principal radii of curvature. This term has the crucial effect that it makes the interface stable against short-wavelength perturbations. The last term on the right-hand-side of Eq. (3) is the non-equilibrium undercooling of the interface that drives crystallization by attachment of atoms at the interface, where $\mu(\hat{n})$ is a kinetic coefficient. The solution of the steady-state growth problem becomes highly non-trivial when the isothermal condition $T = T_M$ is replaced by Eq. (3), and several dendrite growth theories after Ivantsov (reviewed in Ref. [1]) made some uncontrolled approximations that were later proven to be incorrect.

The fundamentally correct solution to this problem emerged in the early nineteen eighties from the study of simplified models where the interface dynamics is governed by local growth laws (a purely geometrical model where V_n depends on the curvature and its second derivative with respect to arclength along the interface [8], and a boundary-layer model [9] that is an approximation of the dendritic growth equations in the limit where the thickness of the thermal diffusion layer surrounding the tip is small compared to ρ). These models had the advantage that they could be simulated numerically and studied analytically without uncontrolled approximations that had been made in previous theoretical attempts to tackle directly the dendrite growth equations with the full non-locality of the diffusion field. Building on insights gained from these studies, solutions to the the full equations were then subsequently obtained in two [10–14] and three dimensions [15, 16].

The key insight gained from these studies is that dendritic evolution is controlled by a delicate balance between microscopic capillary effects and macroscopic heat transport in which the anisotropic properties of the solid-liquid interface play a crucial, and mathematically subtle, role. First, capillary forces act as a singular perturbation that transforms the Ivantsov continuous family of needle crystal solutions into a discrete set of solutions. Second, capillary or/and kinetic effects must be anisotropic for solutions to exist; in this case only the solution with the largest velocity in this discrete set is linearly stable [17] and therefore a potential candidate for the observed dendrite tip.

The self-consistent calculation used to determine this velocity involves a solvability condition, which is simply the condition that a physically admissible solution to the steady-state growth equations must be smooth at the tip. Consequently, the term solvability theory is commonly used to refer to this type of calculation whether it is carried out numerically using a boundary integral approach [11–13, 15] or analytically [10, 14, 16] using a WKB (Wentzel-Kramers-Brillouin) approximation in the limit of weak anisotropy.

Over the last decade, new powerful computational approaches have been developed to simulate the full time-dependent evolution of the solid-liquid interface governed by Eqs. (1)–(3). In particular, the phase-field method [18] has emerged as a powerful algorithm to simulate this evolution in both two and three dimensions [19–26]. This approach has the well-known advantage that it facilitates front tracking by making the phase boundaries spatially diffuse with the help of scalar fields that naturally distinguish between different phases. Using this approach, it has been possible to simulate the morphological development of dendrites and to validate quantitatively that the dynamically selected dendrite tip operating state is indeed the one predicted by solvability theory [22].

Despite this progress, our current ability to model dendritic growth quantitatively for a given material remains very limited. This is mainly due to the lack of knowledge of capillary and kinetic properties ($\gamma(\hat{n})$ and $\mu(\hat{n})$, respectively, which enter through Eq. (3) and, in particular, of their anisotropies that strongly influence the interface dynamics. Exceptions are some transparent organic materials [27–29] and only one metal system (Al-Cu) [30] for which values of the capillary anisotropy have been estimated from experimental measurements of equilibrium shapes. Even for these materials, however, interface kinetic effects have not been quantified even though they could be important. Traditionally, kinetic effects have been assumed to be negligibly small compared to capillary effects at small undercoolings, where the growth rate is small, and the opposite for large undercoolings. However, to predict dendritic evolution over the entire experimentally accessible undercooling range requires a precise knowledge of both capillary and kinetic properties.

The hope to model dendritic evolution quantitatively in metal systems has been recently revived by progress in modeling interfacial properties using large scale molecular dynamics (MD) simulations [31–34]. The interface kinetic coefficient has been calculated for Ni and Cu by crystallizing large slabs of liquid with interatomic potentials derived from the embedded atom method [31]. Values of this coefficient were found to be in good quantitative agreement with a model of Broughton et al. [35] used previously to interpret simulations with the Lennard-Jones potential, and about half an order of magnitude smaller than the value predicted by a model of Turnbull [36] that has been used in the metallurgical literature to model rapid dendritic solidification. Furthermore, the interface kinetics was found to be strongly anisotropic, with growth at the same interface undercooling being faster along [100] than [110], and faster along [110] than [111]. A similar magnitude of anisotropy has also been found in simulations with the Lennard-Jones potential [37].

The anisotropy of the interfacial energy is more difficult to compute for materials with rough interfaces because it is extremely weak, the maximum variation of $\gamma(\hat{n})$ over all orientations $(\hat{n})$ of the interface being typically of the order of one percent. Very recently, however, it has been demonstrated that this anisotropy can be accurately computed by monitoring interfacial fluctuations during MD simulations and extracting the interfacial stiffness, i.e. γ plus its second derivative with respect to orientation in a given plane, which is one order of magnitude more anisotropic than γ itself [32, 33].

The goal of the present work is to model dendritic growth in undercooled metallic melts fully quantitatively by linking atomistic and phase-field simulations. We modify the existing phase-field formulation of the crystallization of a pure melt in order to achieve an efficient and accurate modeling of the large-undercooling regime where interface kinetic effects become important, and we use a recently developed multi-scale algorithm [26] to simulate this model in three dimensions. Furthermore, we use as input into this model the anisotropic capillary and kinetic properties of the solid-liquid interface that have been recently predicted by MD simulations [31, 32]. This allows us to make quantitative predictions of morphological development that can be directly compared with experiments.

We focus on pure Ni for which the interface properties have been most accurately modeled to date by MD simulation. This system also has the advantage of having been extensively studied experimentally. Various groups have measured the relationship between the growth velocity of the interface and the bulk undercooling [38–42]. Moreover, the morphological evolution of the envelope of the solidification front

during recalescence (rapid freezing following triggered nucleation) has been investigated by thermal imaging [41, 42].

We write down the phase-field model and examine its sharp interface limit in Section 2. We then discuss the numerical implementation of this model in Section 3. Next, we discuss the results of phase-field simulations in Section 4. We mainly focus here on the comparison of these results with experimental observations. The comparison with the predictions of solvability theory is only briefly summarized and will be presented in more detail elsewhere. Finally, conclusions and prospects are given in Section 5.

2. Phase-Field Model

2.1. Basic Equations

Over the last decade, the phase-field method [18] has emerged as a powerful computational approach to simulate morphological development during solidification [19–26]. This method has the well-known advantage that it avoids to explicitly track a sharp phase boundary by making the interface region between solid and liquid spatially diffuse over some finite thickness. The general form of the phase-field model that has been widely used to simulate the solidification of a pure melt is defined by the equations

$$\tau(\hat{n})\frac{\partial\phi}{\partial t} = -\frac{\delta F}{\delta\phi}, \tag{4}$$

$$\frac{\partial u}{\partial t} = D\nabla^2 u + \frac{1}{2}\frac{\partial p(\phi)}{\partial t}, \tag{5}$$

where $\delta F/\delta\phi$ denotes the functional derivative with respect to ϕ of the free energy of the two-phase system. The latter assumes the phenomenological form

$$F = \int d\vec{x}\left[\frac{W^2(\hat{n})}{2}|\nabla\phi|^2 + f_{dw}(\phi, u)\right], \tag{6}$$

where the integral in Eq. (6) is over the volume of the system and we have defined the dimensionless temperature field

$$u \equiv (T - T_M)/(L/c_p). \tag{7}$$

Here, f_{dw} is dimensionless and W has dimension of length; consequently, F has dimension of volume. It is important to emphasize that there is a significant amount of freedom in the choice of the functional form of the free energy density $f_{dw}(\phi, u)$ in the phase-field model. The first main requirement is that f_{dw} should have the form of a double well potential with two minima corresponding to the liquid and solid phases, which are chosen here at $\phi = \pm 1$ with the plus (minus) sign corresponding to the solid (liquid). Thermodynamically, this guarantees the existence of a well-defined solid-liquid interface of thickness $\sim W$, i.e. where ϕ varies between $+1$ and -1 over this thickness along a direction that is locally normal to the interface. The second physical requirement is that the difference in bulk free-energy between solid and liquid, which drives the phase transformation, should be a monotonously increasing function of the interface undercooling; this is equivalent, here, to requiring that $f_{dw}(+1, u) - f_{dw}(-1, u)$ be a monotonously increasing function of u. A third requirement is that the two minima of f_{dw} remain at ± 1 for different temperatures above and below the melting point. A choice that satisfies all three requirements is [21–26, 43]

$$f_{dw}(\phi, u) = f(\phi) + \lambda u g(\phi), \tag{8}$$

with λ a dimensionless constant, $f(\phi) = -\phi^2/2 + \phi^4/4$, and

$$g(\phi) = \phi - 2\phi^3/3 + \phi^5/5. \tag{9}$$

This form has been widely used to model dendritic solidification quantitatively in a low undercooling regime where interface kinetic effects are vanishingly small [22, 23, 26]. Here, however, we focus on the opposite high undercooling regime where kinetic effects are dominant. In order to model accurately the kinetics of the interface in this regime, it turns out to be necessary to use the more general form

$$f_{dw}(\phi, u) = f(\phi) + h(\lambda u)g(\phi), \tag{10}$$

which still satisfies the above requirements if h is a monotonously increasing function of its argument. Even on today's computers and with parallel codes, phase-field computations are only feasible for values of W much larger than the real atomic-scale width of the solid-liquid interface, denoted here by δ. With the double well potential defined by Eq. (8) and $W \gg \delta$, the velocity of a planar interface in the phase-field model is a nonlinearly increasing function of the interface undercooling for the high velocity range (30–60 m/sec)

that has been measured experimentally in Ni [38–42]. In contrast, atomistic simulations of the same material [31] have shown that the relationship between the growth rate and the interface undercooling is still linear in this velocity range. This problem can be solved by introducing a function h in the double well potential defined by Eq. (10) that allows one to freely choose the relation between the interface undercooling and the thermodynamic driving force for the phase transformation. Hence, even when the relationship between the interface velocity and the driving force is nonlinear, one can model a linear dependence of the velocity on the interface undercooling. We discuss next how to explicitly compute h and how to choose the parameters in the phase-field model by examining the mapping of this model onto the sharp-interface equations of the previous section. The incorporation of thermal fluctuations into the model is discussed in Section 3 together with the numerical implementation.

2.2. *Relationship Between Phase-Field and Sharp-Interface Models*

To examine the relationship between the phase-field and the sharp-interface equations (Eqs. (1)–(3)), it is useful to first rewrite the latter equations in terms of u, which yields

$$\frac{\partial u}{\partial t} = D\nabla^2 u, \tag{11}$$

$$V_n = D\hat{n} \cdot (\vec{\nabla} u|_S - \vec{\nabla} u|_L), \tag{12}$$

$$u_I = -d_0 \sum_{i=1,2} \left[a_c(\hat{n}) + \frac{\partial^2 a_c(\hat{n})}{\partial \theta_i^2} \right] \frac{1}{R_i} - \beta(\hat{n}) V_n, \tag{13}$$

where we have defined the microscopic capillary length $d_0 \equiv \gamma_0 T_M c_p / L^2$, which is typically on the order of one nanometer, and the kinetic coefficient

$$\beta(\hat{n}) \equiv \frac{c_p}{L\mu(\hat{n})}. \tag{14}$$

Here, γ_0 is the mean value of the interfacial energy that can be defined by writting $\gamma(\hat{n}) \equiv \gamma_0 a_c(\hat{n})$, where the small variation of the interfacial energy with orientation is contained in the dimensionless function $a_c(\hat{n})$ defined in Section 3 below. The interface energy of the phase-field model (which has dimension of length because f_{dw} was chosen dimensionless),

$$\gamma_{pf}(\hat{n}) = W(\hat{n}) \int_{-1}^{1} \sqrt{2[f(\phi) - f(\pm 1)]}\, d\phi, \tag{15}$$

depends only on the shape of the free energy function and is proportional to W. Therefore, anisotropic capillary effects are correctly reproduced in the phase-field model by letting the interface thickness have the same anisotropy as the interfacial energy [19], that is $W(\hat{n}) = W_0 a_c(\hat{n})$ where the direction normal to the interface is defined by $\hat{n} = -\vec{\nabla}\phi / |\vec{\nabla}\phi|$.

The phase-field model is well-known to map onto the above set of sharp-interface equations in the limit where the interface thickness is small compared to the scale of the microstructure. The asymptotic analysis necessary to construct this mapping is rather involved (see Ref. [22] and earlier references therein). We only mention here the main results that are necessary for our computations and to determine h. Let us start with the equilibrium Gibbs-Thomson condition. A curved interface in the phase-field model is stationary only when the temperature u is constant and the driving force induced by the curvature is exactly compensated by the free energy difference between the two bulk phases, $f_{dw}(+1, u) - f_{dw}(-1, u) = \lambda u[g(+1) - g(-1)]$, which yields

$$\lambda u[g(+1) - g(-1)] = -\sum_{i=1,2} \left[\gamma_{pf}(\hat{n}) + \frac{\partial^2 \gamma_{pf}(\hat{n})}{\partial \theta_i^2} \right] \frac{1}{R_i}. \tag{16}$$

Using Eq. (15) and comparing the result to Eq. (13), we deduce that

$$d_0 = a_1 \frac{W_0}{\lambda}, \tag{17}$$

where $a_1 = \int_{-1}^{1} \sqrt{2[f(\phi) - f(\pm 1)]} / [g(+1) - g(-1)]$ is a constant of order unity ($a_1 = 5\sqrt{2}/8$ for the forms of $f(\phi)$ and $g(\phi)$ used here).

Equation (17) implies that for a given capillary length d_0, which is the only fixed length scale in the dendrite growth problem, one has the freedom to vary the interface thickness W_0 in the phase-field model since λ is a free parameter. This freedom is due to the fact that the free-energy difference on the left-hand-side of Eq. (16) is proportional to λ whereas the surface energy on the right-hand-side is proportional to W_0. The goal of choosing W_0 as large as possible in order

to make the phase-field equations less stiff is equivalent to choosing $\lambda \sim W_0/d_0$ as large as possible. How large λ can be chosen, under the constraint that the results be converged (i.e. independent of λ), has been shown to depend on the choice of assumption made in mapping the phase-field model onto the sharp-interface equations [22]. In the classical asymptotic analysis of the *sharp-interface* limit of the phase-field model, λ is assumed to be vanishingly small. This assumption is equivalent, physically, to assuming that the temperature is constant in the diffuse interface region in the limit where its thickness vanishes. The expression for the kinetic coefficient that results from this analysis is

$$\beta(\hat{n}) = a_1 \frac{\tau(\hat{n})}{\lambda W(\hat{n})}. \tag{18}$$

A distinct *thin-interface* limit has also been analyzed where λ is assumed to be of order unity [22]. This analysis computes a correction to the interface kinetics that results from the variation of temperature across the interface width, which is assumed finite (or, in simple terms, the interface is assumed to be "thin" as opposed to sharp). This analysis yields the modified expression for the kinetic coefficient [22]

$$\beta(\hat{n}) = a_1 \frac{\tau(\hat{n})}{\lambda W(\hat{n})}\left[1 - a_2 \lambda \frac{W^2(\hat{n})}{D\tau(\hat{n})}\right], \tag{19}$$

where a_2 is a constant of order unity that depends again on the functional forms of the functions $f(\phi)$ and $g(\phi)$ ($a_2 = 0.6267$ for the forms used here). This expression has the advantage that it remains valid for larger λ than the one derived in the classical sharp-interface limit. Furthermore, it can even be used to make the interface kinetics vanish by choosing $\tau(\hat{n}) = \lambda a_2 W^2(\hat{n})/D$, which makes the square bracket in Eq. (19) vanish.

In the early stage of the present investigation, we used the standard form of the double well potential given by Eq. (8) to simulate dendritic evolution in two dimensions for the parameters of pure Ni discussed below, together with Eqs. (17) and (19) to interpret the results. We investigated values of $\Delta T/(L/c_p)$ varying between 0.2 and 0.6, which is the undercooling range of interest to make contact with experiments. We found that the dendrite tip velocity only became independent of the interface thickness for λ of order unity, which is equivalent to choosing this thickness comparable to the atomic-scale width δ of the real solid-liquid interface. These simulations turned out to be extremely costly and not feasible in three dimensions. The results of the simulations were analyzed in order to elucidate the cause of this poor convergence. Plots of the temperature profile along the central axis of the dendrite revealed that the magnitude of the temperature variation across the diffuse interface is small compared to the magnitude of the total interface undercooling. The latter is itself a significant fraction of the total bulk undercooling at this large growth rate. Consequently, the correction to the kinetic coefficient predicted by the thin-interface limit is essentially negligible. This is easily seen by rewriting Eq. (19) in the form

$$\beta = \beta_0\left[1 - a_2 \lambda \frac{d_0}{D\beta_0}\right], \tag{20}$$

using Eq. (17), where β_0 denotes the kinetic coefficient predicted by the sharp-interface limit (Eq. (18)), and where we have neglected anisotropy for simplicity. For the parameters of pure Ni predicted by the MD simulations [31], $d_0/(D\beta_0) \approx 1/90$, such that the second term inside the square bracket in Eq. (20) is small compared to one for λ of order unity.

Further analysis of the results revealed that the linear relationship between interface undercooling and velocity, $u_I = -\beta V_n$, breaks down for the velocity range of interest here. Since only the product λu enters the phase-field equation, this breakdown occurs at smaller velocity as λ is increased. This explains the dependence on λ of our dendrite simulation results with f_{dw} defined by Eq. (8). To overcome this difficulty, we use the new form of f_{dw} defined by Eq. (10). The velocity of a planar interface is uniquely related to the driving force, which is $-\lambda u_I$ in Eq. (8), but $-h(\lambda u_I)$ in Eq. (10). Hence, once we have determined the nonlinear relationship between the interface velocity and h, we can then choose $h(\lambda u_I)$ so as to recover a linear relationship between interface velocity and u_I. Let us first compute the nonlinear relationship between the interface velocity and h. This can be done by rewriting Eq. (4), with f_{dw} defined by Eq. (10), in a frame translating along the $+x$ direction at velocity V_n and by making the change of variable $y = x/W(\hat{n})$, which yields

$$v\frac{d\phi}{dy} + \frac{d^2\phi}{dy^2} - f'(\phi) - hg'(\phi) = 0, \tag{21}$$

where we have defined the dimensionless interface velocity $v = V_n\tau(\hat{n})/W(\hat{n})$ and the primes on f and g denote differentiation with respect to ϕ. Physically admissible solutions of Eq. (21) that exhibit a smooth and monotonous variation of ϕ across the diffuse interface

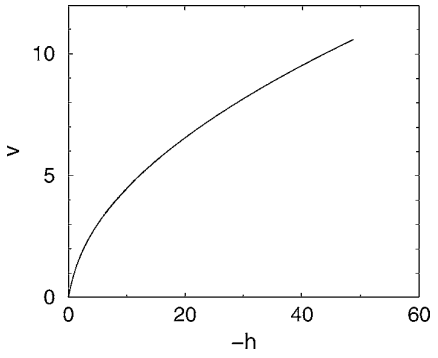

Figure 1. Plots of the dimensionless interface velocity v of an isothermal planar interface versus driving force $-h$ in the phase-field model.

only exist for a unique v for a given value of h. They can be found by first writing Eq. (21) as a set of two coupled first-order differential equations, and then using a shooting method to find the value of v that satisfies the boundary conditions $\phi(\pm\infty) = \mp 1$. By repeating this procedure for different values of h, one can compute the function $v(h)$, which we plot in Fig. 1. To make the interface kinetics linear for large λ, it now suffices to choose the function $h(\lambda u_I) = v^{-1}(-\lambda u_I/a_1)$, where v^{-1} is the inverse of the function v. This inverse function is uniquely defined because v is a monotonous function of its argument. Consequently, $v(h(\lambda u_I)) = v(v^{-1}(-\lambda u_I/a_1)) = -\lambda u_I/a_1$, such that finally

$$V_n = \frac{W(\hat{n})}{\tau(\hat{n})} v(h(\lambda u_I)) = -u_I/\beta(\hat{n}), \tag{22}$$

where $\beta(\hat{n})$ is given by Eq. (18), as desired. For modeling dendrites, the magnitude of λu_I only becomes large when the interface is undercooled ($u_I < 0$), whereas this magnitude is small during melting ($u_I > 0$), e.g. the remelting of secondary branches. Therefore, we choose $h(\lambda u_I) = v^{-1}(-\lambda u_I/a_1)$ for $u_I < 0$ and $h(\lambda u_I) = \lambda u_I$ for $u_I > 0$. Finally, by extending the above analysis to a moving curved interface, it can also be shown that the Gibbs-Thomson condition with a linear kinetic correction term (Eq. (13)) is correctly reproduced with the new form of f_{dw} defined by Eq. (10).

3. Numerical Implementation

In summary, we simulate the phase-field model defined by Eqs. (4) and (5) together with the double-well potential defined by Eq. (10), $f(\phi) = -\phi^2/2 + \phi^4/4$, $g(\phi)$ defined by Eq. (9), the function $h(\lambda u)$ defined by $h(\lambda u) = \lambda u$ for $\lambda u > 0$ and constructed, for $\lambda u < 0$, from the inverse of the function $v(\lambda u)$ computed by solving Eq. (21) as outlined above; values of h for $\lambda u < 0$ are tabulated beforehand at equally spaced intervals and h is computed by simple linear interpolation from these tabulated values during the simulations. The interfacial energy and the kinetic coefficient are assumed to have the forms

$$\gamma(\hat{n})/\gamma_0 \equiv a_c(\hat{n}) = (1 - 3\epsilon_c) \times \left[1 + \frac{4\epsilon_c}{1 - 3\epsilon_c}\left(n_x^4 + n_y^4 + n_z^4\right)\right], \tag{23}$$

$$\beta(\hat{n})/\beta_0 \equiv a_k(\hat{n}) = (1 + 3\epsilon_k) \times \left[1 - \frac{4\epsilon_k}{1 + 3\epsilon_k}\left(n_x^4 + n_y^4 + n_z^4\right)\right], \tag{24}$$

consistent with the symmetry of a crystalline material with an underlying cubic symmetry, where ϵ_c (ϵ_k) is the magnitude of the capillary (kinetic) anisotropy. With the above definitions, a positive value of ϵ_c (ϵ_k) favors growth along the [100] directions, which requires the interfacial energy (kinetic coefficient) to be maximal (minimal) along these directions. Using the definition $W(\hat{n}) = W_0 a_c(\hat{n})$ together with Eqs. (17) and (18), we obtain

$$W(\hat{n}) = \frac{8\lambda d_0}{5\sqrt{2}} a_c(\hat{n}) \tag{25}$$

$$\tau(\hat{n}) = \frac{32\lambda^2 d_0 \beta_0}{25} a_c(\hat{n}) a_k(\hat{n}) \tag{26}$$

that are integrated in the phase-field model using $\hat{n} = -\vec{\nabla}\phi/|\vec{\nabla}\phi|$, or

$$n_x^4 + n_y^4 + n_z^4 = \frac{(\partial\phi/\partial x)^4 + (\partial\phi/\partial y)^4 + (\partial\phi/\partial z)^4}{|\vec{\nabla}\phi|^4} \tag{27}$$

in Eqs. (23) and (24).

Thermal fluctuations are incorporated into the model by using the standard Langevin formalism that has been widely used in studies of second order phase transitions [44], and more recently in phase-field models of solidification [25, 45, 46]. This formalism consists in adding random variables to the right-hand side of the phase-field equations, with the noise in Eq. (5) written in such a way that the total heat is conserved. These random

variables are chosen to be uncorrelated in space and time and to obey Gaussian distributions whose variances are dictated by the fluctuation-dissipation theorem. This formalism has been used previously by Karma and Rappel [25] to investigate the formation of sidebranches in dendritic solidification, and we follow here exactly the same procedure to include fluctuations. The variances of the non-conserved and conserved noises added to Eqs. (4) and (5), respectively, are determined by a single dimensionless experimental parameter

$$F_{expt} = \frac{k_B T_M^2 c_p}{L^2 d_0^3}, \tag{28}$$

where k_B is the Boltzmann constant, as detailed in Ref. [25].

Our simulations exploit a hybrid finite-difference diffusion Monte Carlo algorithm that integrates efficiently the phase-field equations [26]. In a first domain D_1, consisting of the solid plus a thick liquid layer surrounding the solid-liquid interface, the stochastic phase-field equations (with the Langevin noise added to both equations as in [25]) are time-stepped using a standard explicit Euler method with a finite-difference representation of the spatial derivatives on a cubic lattice. In a second domain D_2, consisting of the rest of the liquid, Eq. (5) reduces to the heat diffusion equation that is solved using a large ensemble of random walkers. The walkers make progressively larger steps with increasing distance away from the interface, and this adaptive stepping reduces the computer time in a way that is similar to adaptive meshing algorithms. The two methods are interfaced at the conversion boundary between domains D_1 and D_2 in such a way that heat is exactly conserved.

All the details of this algorithm are described in Ref. [26] and need not be reproduced here. In addition, the finite-difference implementation of the phase-field equations in D_1, which was used in Ref. [26], has been described in detail in Ref. [22]. Here we make two additional improvements to this implementation. First, we integrate the equation for u (Eq. (5)) in D_1 on a twice coarser mesh than the equation for ϕ (Eq. (4)); values of u on the fine mesh are then simply calculated by interpolating between values of u on the coarse mesh. Numerical tests show that this approach gives essentially identical results as using a single mesh. Second, we write the evolution equation for ϕ derived from Eq. (4) by inserting all the anisotropic factors in the form

$$\begin{aligned}\tau(\hat{n})\partial_t\phi = {} & W_0^2\nabla^2\phi + \vec{\nabla}\cdot\left(\left[W(\hat{n})^2 - W_0^2\right]\vec{\nabla}\phi\right) \\ & + \sum_{w=x,y,z}\frac{\partial}{\partial w}\left(|\vec{\nabla}\phi|^2 W(\hat{n})\frac{\partial W(\hat{n})}{\partial[\partial\phi/\partial w]}\right) \\ & + (\phi - h(\lambda u)(1-\phi^2))(1-\phi^2),\end{aligned} \tag{29}$$

where the second and third terms on the right-hand side above vanish in the isotropic limit $\epsilon_c \to 0$. The spatial derivatives associated with these terms are discretized using centered finite-difference expressions, as before [22]. In contrast, the isotropic Laplacian (first term on the right-hand-side above) is discretized using the 18-point formula

$$\nabla^2\phi|_{i,j,k} = \frac{1}{3\Delta x^2}\left[\sum_{nn}\phi + \frac{1}{2}\sum_{nnn}\phi - 12\phi_{i,j,k}\right], \tag{30}$$

where $\sum_{nn}\phi$ and $\sum_{nnn}\phi$ denote the sums of ϕ-values evaluated at the 6 nearest-neighbor and the 12 next-nearest-neighbor positions on the cubic lattice, respectively, where Δx is the lattice spacing (equal along x, y, and z). The key property of this 18-point formula is that it makes the lattice corrections to the lowest order forms of the capillary and kinetic anisotropies defined by Eqs. (23) and (24) vanish at order Δx^2. This can be seen by performing a Taylor expansion in Δx of the discretized Laplacian. For planar interfaces parallel to the (100), (110), and (111) planes this expansion reduces to the form $\nabla^2\phi \approx \partial^2\phi/\partial n^2 + A(\Delta x)^2\partial^4\phi/\partial n^4 + O(\Delta x^4)$, where n is the coordinate normal to the interface, and A is a numerical constant. For the 18-point formula, A is *identical* for all three planes. In contrast, A has a different value in each plane if the Laplacian is discretized using the standard finite-difference expression that only involves the nearest-neighbor sum. This, in turn, generates order Δx^2 lattice corrections to the capillary and kinetic anisotropies that can be taken into account following the estimation procedure developed in Ref. [22]. The use of Eq. (30) eliminates the need for this procedure to resolve small physical anisotropies and pushes anisotropic effects due to the lattice discretization to a higher order (Δx^4) where numerical tests show that they are small enough to be neglected.

Let us briefly comment on the sources of noise in our present numerical algorithm. The noise produced by the random walkers is only generated in

D_2, whereas the Gaussian thermal noise that is added through stochastic variables in the phase-field equations is only generated in D_1. It was shown in Ref. [26] that the walker noise has a negligible effect on the interface evolution because its magnitude decreases by several orders of magnitude across the liquid layer surrounding the interface. Most importantly, this noise is insufficient to sustain sidebranching. One issue, however, is whether adding stochastic forces to the phase-field equations only in region D_1 (as opposed to the entire computation domain $D_1 + D_2$, as would be the case if we had used a finite-difference scheme everywhere) reduces the strength of the thermal noise in a degree that affects the results. To investigate this issue numerically, we repeated certain test simulations with different values for the thickness of the liquid layer surrounding the interface, and found that the sidebranch amplitude remained approximately the same provided that this thickness is chosen large enough (about 25–50 times the width of the diffuse interface in the present study). Therefore, we conclude that our results are not significantly affected by only adding Langevin noise in D_1.

We use for material parameters of pure Ni: $T_M = 1726$ K, $L = 2.311 \times 10^9$ J/m^3, $c_p = 5.313 \times 10^6$ J/(m^{3}K), $D = 10^{-5}$ m^2/sec, $\gamma_0 = 0.326$ J/m^2, $\epsilon_c = 0.018$, $\mu_{100} = 0.52$ m/sec, and $\mu_{110} = 0.40$ m/sec, where the capillary and kinetic parameters have been estimated by monitoring the fluctuations of the solid-liquid interface during MD simulations [31, 47]. From these values, we obtain $L/c_p = 435$ K, $d_0 = 5.56 \times 10^{-10}$ m, $\beta_0 = c_p(1/\mu_{100} + 1/\mu_{110})/(2L) = 5.084 \times 10^{-3}$ sec/m, $\epsilon_k = (\mu_{100} - \mu_{110})/(\mu_{110} + \mu_{110}) = 0.13$, and $F_{expt} = 0.234$.

Simulations were carried out on a $800 \times 520 \times 520$ lattice with the (100) growth direction along the larger dimension. We fully exploited the cubic symmetry of the crystal to reduce the computation time as described in [26]. Furthermore, we used a spacing $\Delta x = 0.8 W_0$ and a time step $\Delta t = 0.004\,\tau_0$, where $W_0 = 8\lambda d_0/(5\sqrt{2})$ and $\tau_0 = 32\lambda^2 d_0 \beta_0/25$. Note that the physical domain being simulated is actually the sum of the two aforementioned domains D_1 and D_2, and D_2 extends farther than the lattice because the walkers make unrestricted off-lattice walks. We used as initial condition a small spherical seed and followed the morphological development of the interface up to the point where D_1 is no longer contained inside the 3-d lattice. This allowed sufficient time for the dendrite tip to reach a steady-state velocity in the simulations for the parameters studied. Finally, we increased λ from 2 to 16 as $\Delta T/(L/c_p)$ was decreased from 0.8 to 0.2, which yielded converged results that are reasonably independent of interface thickness (i.e. of λ).

4. Results and Discussion

4.1. Comparison with Experiments

We compare in Fig. 2 the variation of the steady-state dendrite growth velocity with bulk undercooling obtained from the phase-field simulations with two sets of experimental measurements [39, 42]. These measurements were made on small high-purity Ni droplets (a few millimeters in diameter) using a widely used experimental technique that consists of electromagnetically levitating the droplets in order to avoid container-wall-induced heterogeneous nucleation, which is essential to attain very large undercoolings.

In these experiments, crystallization of the undercooled melt is externally initiated by mechanical contact between the liquid droplet and a trigger needle at a well-defined undercooling. After nucleation, the solidification front propagates outwards from the trigger point throughout the bulk of the droplet. The velocity of this front is measured by recording the abrupt change of surface temperature that is produced by its passage. Willnecker et al. [39] measured the temperature with photodiodes in two regions of the droplet and obtained an average measure of the velocity from the time difference of the arrival of the front. Lum et al. [41] and

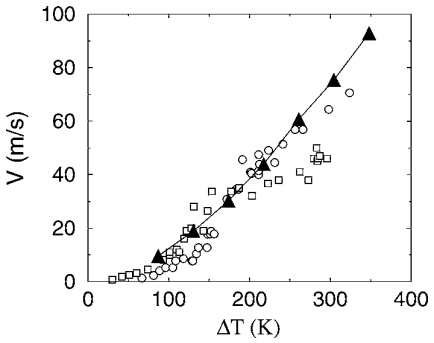

Figure 2. Dendrite velocity versus undercooling from two sets of experiments in Ni by Lum et al. [41] (open squares) and Willnecker et al. [39] (open circles), and from the phase-field simulations (filled triangles and solid line) with $\lambda = 16$, 12, 8, 5, 4, 3, and 2 for $\Delta T/(L/c_p) = 0.2$, 0.3, 0.4, 0.5, 0.6, 0.7, and 0.8, respectively, and with the anisotropy parameters $\epsilon_c = 0.018$ and $\epsilon_k = 0.13$ estimated by atomistic simulations for pure Ni [31, 32].

Matson [42] used a fast high-resolution video camera that images the thermal profile of the entire surface and that provides, in addition to the velocity, information about the morphological evolution of the solidification front.

The comparison in Fig. 2 shows that the phase-field model predictions are in reasonably good quantitative agreement with the measured values of the velocity up to a critical undercooling $\Delta T_c \approx 200$ K. For $\Delta T > \Delta T_c$, the measured solidification velocity increases more slowly with undercooling than predicted by the model, especially for the data set of Lum et al. [41] and Matson [42]. This break in the slope of the measured $V - \Delta T$ curve, which is absent in the simulations, was first seen by Walker [38], and its existence has since been confirmed by numerous experiments [39–42].

From the analysis of the thermal imaging data, Lum et al. [41] and Matson [42] have concluded that this break is correlated with a change of morphology of the envelope of the solidification front, from angular for $\Delta T < \Delta T_c$, to spherical for $\Delta T > \Delta T_c$. Note that the spatial resolution of these images (64×64 pixels over an area of a few millimeter square) is far too coarse to image directly the interface on the scale of the dendrite tip, which is in the submicron range for these high undercoolings. Therefore, these images track the evolution of the macroscopic envelope of the solidification front, but not of the front itself.

At these high growth rates, the thickness of the thermal diffusion boundary layer (which scales as D/V) is small enough for the tips of surviving secondary branches to grow independently, and at the same rate as primary branches. Moreover, since secondary branches grow at 90° from the trunks of primary dendrite branches sufficiently behind the tip, one would expect the envelope of the solidification front associated with steady-state dendrite growth along the [100] directions to be pyramidal, or angular once projected onto the droplet surface being imaged, as observed in Ref. [42]. In contrast, the observation of a transition to a smooth spherical envelope suggests that steady-state dendrite growth along a preferred crystallographic direction no longer exists for $\Delta T > \Delta T_c$.

Our phase-field simulations show no indication of the existence of such a transition with the present parameters used for Ni. The growth morphology remains dendritic, with a well-defined steady-state tip velocity, even for the largest simulated undercooling that is larger than ΔT_c in the experiments. Examples of growth morphologies are shown in Fig. 3(a) and (b). Much larger size simulations, which are not feasible in three dimensions, would be necessary to describe the dynamics of the envelope of the solidification front on the scale where it has been imaged experimentally. However, we expect this envelope to be pyramidal over the entire range of undercoolings investigated here in view of the smooth $V - \Delta T$ curve and the persistence of a stable dendrite tip for $\Delta T > \Delta T_c$. Larger size simulations conducted in two dimensions for the same parameters confirm this expectation.

4.2. *Sensitivity to Anisotropy and Kinetic Effects*

In order to investigate the source of the disagreement between simulations and experiments for $\Delta T > \Delta T_c$, and also to gain insight into the factors controlling the interface dynamics, we carried out additional simulations by varying independently the magnitude of the capillary and kinetic anisotropy. Varying the magnitude of the capillary anisotropy (ϵ_c) was found to have very little influence on the results. This is shown in Fig. 4 where we compare the phase-field simulation results for the value $\epsilon_c = 0.018$ estimated for Ni [31] and for $\epsilon_c = 0$, corresponding to a purely isotropic interfacial energy. The dendrite velocities are almost identical over the whole range of undercooling investigated.

In contrast, we found that both the solidification rate and the growth morphology depend sensitively on the magnitude of the kinetic anisotropy (ϵ_k) that was varied for a fixed value of the capillary anisotropy $\epsilon_c = 0.018$. This is shown in Fig. 5 where we plot the computed dendrite velocity as a function of ϵ_k at a fixed undercooling. The velocity is seen to decrease as ϵ_k is lowered. Moreover, steady-state growth ceases to exist for ϵ_k less than a critical value ϵ_k^* that varies from zero to about 0.02 for $\Delta T/(L/c_p)$ varying from about 0.2 to 0.7 as shown in Fig. 6. We note that ϵ_k^* should also depend on the capillary anisotropy that does not influence the interface dynamics when ϵ_k is large, as already mentioned, but that does compete with the kinetic anisotropy when ϵ_k is small (i.e. comparable to ϵ_k^*). In particular, increasing ϵ_c shifts to higher undercoolings the region where steady-state dendrite growth ceases to exist in the ϵ_k-ΔT plane of Fig. 6.

For $\epsilon_k < \epsilon_k^*$, interface growth is dominated by tip-splitting, which produces new branches, and branch-termination by overgrowth from neighboring branches. Since the branches do not have any obvious preferred growth direction, the envelope of the interface on a

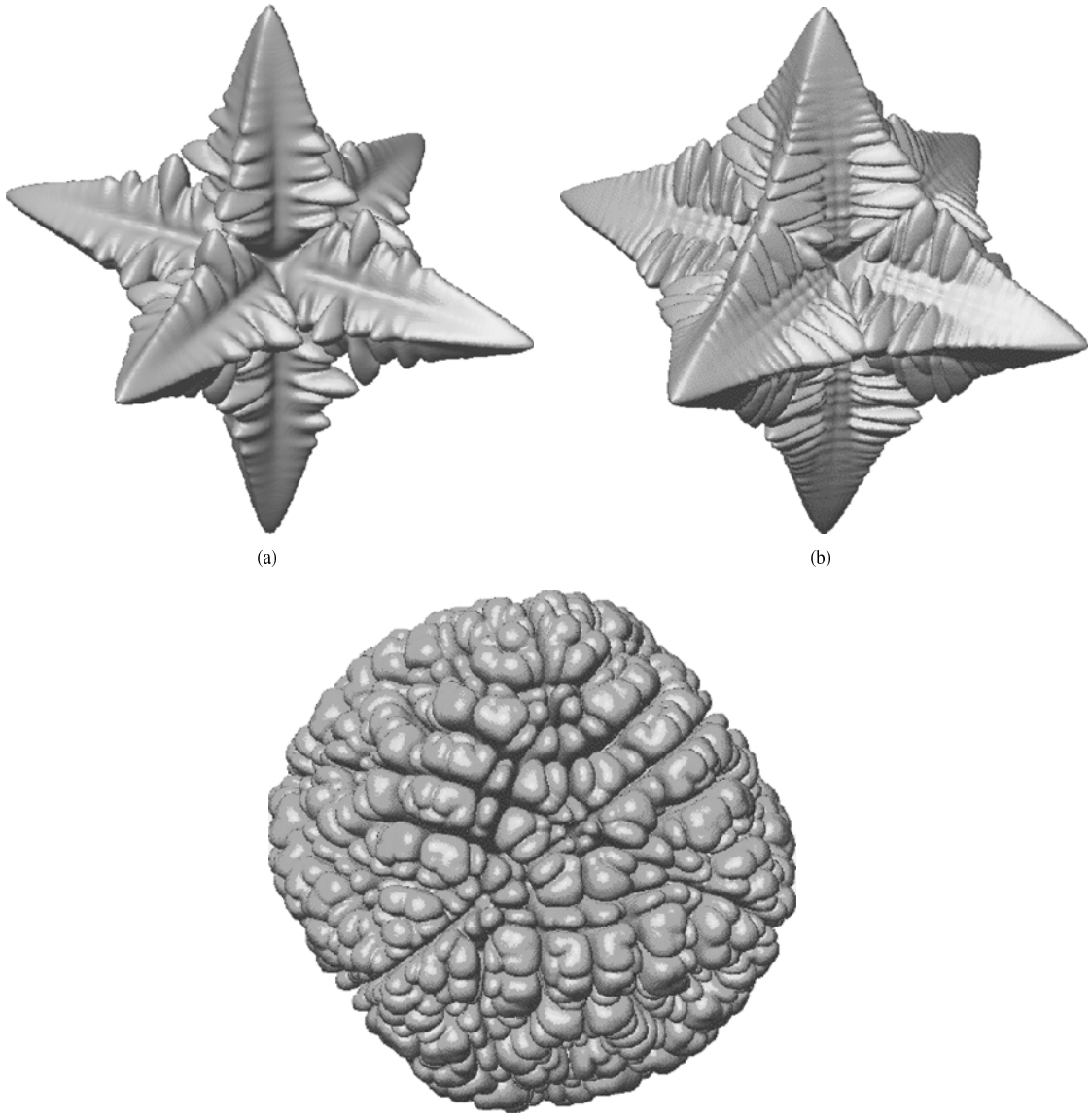

Figure 3. Snapshots of 3-d interfaces for different anisotropy parameters: (a) $\lambda = 30$, $\epsilon_k = 0.13$, $\epsilon_c = 0.018$, and $\Delta T/(L/c_p) = 0.2$; (b) $\lambda = 20$, $\epsilon_k = 0.13$, $\epsilon_c = 0.018$, and $\Delta T/(L/c_p) = 0.7$; (c) $\lambda = 20$, $\epsilon_k = 0$, $\epsilon_c = 0.018$, and $\Delta T/(L/c_p) = 0.6$. Larger values of λ were used in these simulations to obtain more developed structures for illustrative purposes.

scale larger than the average branch spacing becomes progressively more spherical as one moves away from the boundary that marks the lower limit of existence of dendrite growth in the ϵ_k-ΔT plane of Fig. 6. This is illustrated in Fig. 7 that shows space-time plots of the interface for two extreme values of ϵ_k at fixed ΔT. An example of a 3-d spherical envelope morphology is shown in Fig. 3(c). This structure is qualitatively similar to the so-called dense-branching morphology characteristic of diffusion-limited growth with tip-splitting [48]. This morphology has been observed in a wide range of systems, including two-dimensional viscous flow in a Hele-Shaw cell and amorphous annealing [48]. Figure 4 shows that the average velocity of the

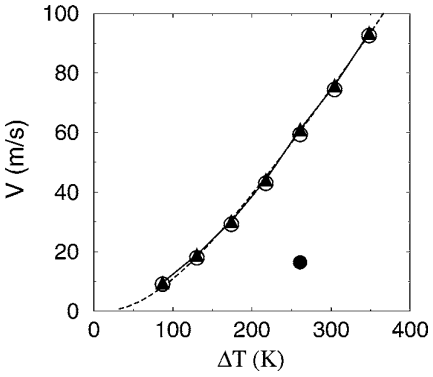

Figure 4. Dendrite velocity versus undercooling obtained from the phase-field simulations for $\epsilon_k = 0.13$ and $\epsilon_c = 0.018$ (filled triangles and solid line), $\epsilon_k = 0.13$ and an isotropic interfacial energy $\epsilon_c = 0$ (open circles), and average velocity of the dense-branching morphology with $\epsilon_k = 0$ and $\epsilon_c = 0.018$ (filled circle). The predictions of solvability theory (thick dashed line) for $\epsilon_k = 0.13$ and $\epsilon_c = 0.018$ agree quantitatively with the simulations.

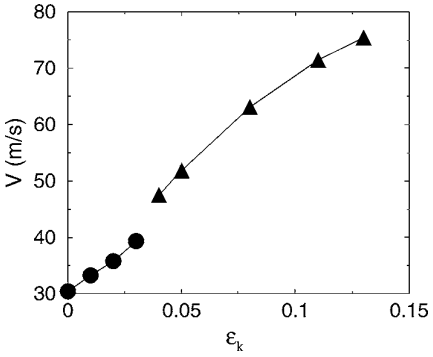

Figure 5. Dendrite tip velocity (filled triangles) and average velocity of the envelope of the interface (filled circles) versus kinetic anisotropy for $\lambda = 4$, $\epsilon_c = 0.018$, and $\Delta T/(L/c_p) = 0.7$.

envelope of this morphology is much slower here than the tip velocity of a dendrite grown at the same undercooling with a large kinetic anisotropy.

The above results show that the interface dynamics is strongly influenced by kinetic effects. This is due to the fact that, for the large growth rates investigated here, the interface kinetic undercooling ($\Delta T_I = \mu_{100} V$) is a significant fraction of the total bulk undercooling, whereas the curvature undercooling associated with capillary forces can be estimated to be one to two orders of magnitude smaller than ΔT_I from the computed values of the tip radius. Of course, one would expect the opposite to be true for low undercoolings, but we have not investigated this range here for the parameters of Ni.

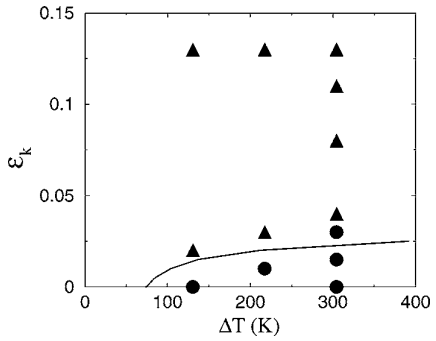

Figure 6. Growth morphology diagram showing the region of existence of dendrite (filled triangles) and dense-branching (filled circles) morphologies in the plane of kinetic anisotropy and undercooling for the phase-field simulations with $\epsilon_c = 0.018$. For the same parameters, solvability theory predicts that steady-state dendrite growth solutions only exist above the solid line, in reasonably good quantitative agreement with the phase-field results.

4.3. *Comparison with Solvability Theory and Previous Numerical Studies*

The phase-field results are in good quantitative agreement with the predictions of an analytical solvability theory developed by Lee et al. that includes both capillary and kinetic effects [49, 50]. This theory is a direct extension of the linearized solvability theory developed previously by Barbieri and Langer [14], which included only capillary effects. In the theory of Lee et al., the steady-state growth equations are linearized around a paraboloid of revolution and solved using a WKB approximation. The resulting solvability condition for the existence of a smooth dendrite solution is expressed in the form of a vanishing integral condition where the integral is evaluated numerically. Details of this theory will be presented elsewhere and we only summarize here the main results.

We compare in Fig. 4 the dendrite velocity-undercooling curve predicted by this theory, for the same parameters of Ni as used in the phase-field model, to the simulation results. The agreement is remarkably good given the fact that the tip shape significantly deviates from a paraboloid of revolution in this growth regime dominated by anisotropic kinetics. Furthermore, this theory predicts that dendrite growth ceases to exist in a region of the $\epsilon_k - \Delta T$ plane that is below the solid curve in Fig. 6 and that is in reasonably good quantitative agreement with the phase-field results. The breakdown of the dendrite solution occurs

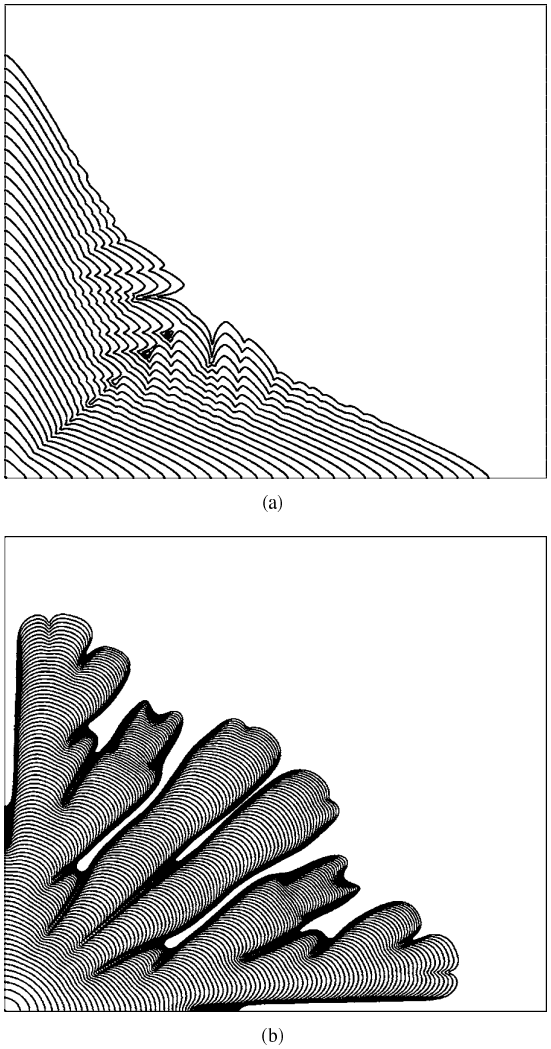

(a)

(b)

Figure 7. Plots of interface evolution for strongly anisotropic (a) and isotropic (b) kinetics. Interfaces in (a) and (b) were extracted from the same simulations that produced the dendrite and dense-branching morphology shown in Fig. 3(b) and (c), respectively. The interfaces represent cuts of the solid-liquid interface in a plane perpendicular to the [010] direction and are shown at equal time intervals. The frame width and height are both 8 μm in (a) and (b).

because the main steady-state dendrite branch merges with a lower-velocity unstable branch at a critical undercooling. Hence, dendrites only exist below this critical undercooling as shown in the morphology diagram of Fig. 6.

It should be emphasized that the transition from dendritic growth to dense-branching morphology with increasing undercooling is fundamentally different in the present kinetic-dominated regime than in the opposite capillary-dominated regime that has been previously investigated in both 2-d [51] (with earlier references therein) and 3-d [52]. In the latter regime, the disappearance of dendrites has been shown to be associated with noise-induced tip splitting [51], or with the appearance of other branches of steady-state solutions with a split tip [51, 52]. In 2-d, the building block of the dense-branching or seaweed morphology is the so-called doublon [51] consisting of two asymmetric fingers that grow cooperatively. In a capillary dominated growth regime, doublons exist above a critical undercooling that depends on the magnitude of the capillary anisotropy. Beyond that threshold, the main steady-state branch of dendrite solutions still exists, but doublons grow faster and outrun dendrites. In 3-d, for growth in a channel, a triplet structure consisting of three asymmetric fingers has been found in numerical simulations [52]. No detailed quantitative study has been carried out, but it might be expected that, qualitatively, triplets play the same role in 3-d as doublons in 2-d. In contrast, in the present kinetic-dominated regime, we have seen no evidence of doublons (triplets) in our 2-d (3-d) phase-field simulations. Consequently, the emergence of the dense-branching morphology is directly linked to the *termination* of the main dendrite steady-state branch at some critical undercooling [50].

To further check this conclusion, we repeated *without noise* the phase-field simulations corresponding to isotropic kinetics and high undercoolings in the morphology diagram of Fig. 6. We found that tip splitting still occurred. Hence, we conclude that noise is not required here to induce splitting. It is probable that noise shifts the critical undercooling at which splitting occurs, but we have not conducted an exhaustive (and numerically intensive) study to determine the magnitude of this shift. The relatively good agreement between solvability and phase-field results in Fig. 6 suggests that this shift is small.

In a recent 3-d phase-field simulation study that focused on a capillary-dominated regime without kinetics [53], we found that the dendrite tip was destroyed by thermal noise above a critical undercooling of about half the hypercooling limit that roughly coincides with ΔT_c in the pure Ni experiments. Furthermore, we conjectured that this noise-induced tip splitting behavior could potentially explain the universally observed break in the $V - \Delta T$ curve, *if* it persists in the presence of kinetic effects [53].

The present study clearly demonstrates that noise-induced tip splitting is prevented by strongly anisotropic kinetics for the values of β_0 and ϵ_k estimated in the MD simulations, which invalidates this hypothesis. It is possible that the values of these parameters could vary somewhat if the MD simulations were to be repeated with more accurate interatomic potentials. However, ϵ_k would have to be reduced by about one order of magnitude for a transition from dendrites to a spherical growth morphology to occur with increasing undercooling according to the results of Fig. 6. Moreover, since the phase-field results do agree quantitatively with experiments for $\Delta T < \Delta T_c$, ϵ_k would have to decrease abruptly close to ΔT_c to explain the data, which seems unlikely.

Another possibility is that β_0 is not correctly estimated by the atomistic simulations, and that the model could match the data over the whole undercooling range for a smaller value of β_0 and a very weak kinetic anisotropy. This also seems unlikely because β_0 has been extracted from MD simulations with different methods and potentials, which have all yielded results consistent with the Broughton-Gilmer-Jackson (BGK) model [35]. What remains more uncertain is the magnitude of the kinetic anisotropy.

Very recently, Mullis and Cochrane [54] carried out 2-d phase-field simulations of the crystallization of a pure melt using an estimate of β_0 based on the Turnbull model [36] that is several times smaller than the value predicted by MD simulations or the BGK model [35]. They also used a very weak kinetic anisotropy induced by the orientation dependence of the interface thickness in the phase-field model. They found that, for these kinetic parameters, dendrites are destroyed by noise and replaced by a seaweed structure at large growth rate. Furthermore, they conjectured, as in Ref. [53], that this noise-induced tip splitting could be the mechanism of the envelope transition observed by Matson [42]. Again, the present study invalidates this hypothesis, at least for pure melts, under the assumption that the kinetic parameters predicted by the MD simulations are correct.

Finally, the disappearance of the dendrite branch was not seen in a previous numerical solvability calculation by Ben Amar [55] with isotropic kinetics ($\epsilon_k = 0$). The reason is that a much smaller kinetic coefficient was used ($\beta_0 D/d_0 \approx 15$ in Ref. [55] instead of $\beta_0 D/d_0 \approx 90$ here), which extends the steady-state dendrite branch to higher undercoolings.

4.4. *Effects not Included in the Model*

If we assume that the existing MD estimates of interface kinetic parameters are correct, then the most interesting conclusion from the present study is that other physical effects neglected here influence the interface dynamics for $\Delta T > \Delta T_c$. Since we have used a phase-field model that describes the crystallization of a pure substance with only diffusive transport in the melt, two possible candidates are fluid flow and the presence of very dilute impurities in the melt, which are both unavoidably present in experiments.

An analytical study of flow has been carried out by Horvay [56], motivated by experimental observations by Walker [57] in pure Ni. He concluded that the negative pressure generated by the density difference between solid and liquid should suffice to induce cavitation during the very initial stage of crystallization after nucleation. Although this phenomenon may be unrelated to the observed morphology transition, it raises the issue of whether fluid flow could modify sufficiently the conditions at the interface (during the subsequent stage where the entire melt crystallizes) to alter the MD estimates of kinetic parameters, and consequently the phase-field predictions.

Although the experiments to which we have compared our phase-field results used high purity Ni (e.g. better than 99.99% in Ref. [39]), some small amount of contamination may play a role. Recently, Cochrane et al. have investigated the effect of the oxygen content on the velocity-undercooling curve in Cu [58]. They found that the typically observed break in the slope of this curve was absent for an oxygen content less than 200 ppm, but present for Cu doped with 600 ppm of O. Furthermore, there is significant variation in the $V - \Delta T$ curves reported from various experiments in Ni (see Fig. 1 in Lum et al.), which could potentially result from oxygen contamination.

Even very dilute amounts of impurities can strongly influence the interface dynamics because solutal diffusion in the liquid is about four orders of magnitude slower than heat diffusion. In addition, impurities are known to be trapped by the rapidly advancing interface for the velocities corresponding to the undercooling range studied here [59]. This solute trapping effect need not be isotropic. If it is sufficiently anisotropic, it could potentially alter the interface dynamics. To our knowledge, however, nothing is known either experimentally or theoretically about this anisotropy in metallic alloys.

5. Conclusions

The crystallization of highly undercooled Ni melts was modeled using a computationally efficient phase-field approach together with capillary and kinetic properties of the solid-liquid interface that have been recently estimated by atomistic simulations [31, 32]. In particular, the value used here for the kinetic coefficient (β_0) is much larger than the estimate of the Turbull model [36] that has been traditionally used to model dendrite growth at high undercooling. Consequently, the interface dynamics is much more strongly dominated by kinetics, and our results are drastically different from those obtained in previous studies based on the Turbull estimate [41, 42, 54, 55] or in related studies that focused on a purely capillary-dominated regime without kinetics [51, 53].

The dependence of dendrite growth velocity on undercooling predicted by the phase-field simulations is in good quantitative agreement with experimental data for $\Delta T < \Delta T_c$, where ΔT_c is the critical undercooling corresponding to a break in the slope of the measured $V - \Delta T$ curve. For $\Delta T > \Delta T_c$, the velocity increases more rapidly with undercooling in the simulations, which do not show this break, than in the experiments. Furthermore, the simulations predict that dendrite growth persists even for the largest undercoolings that have been studied experimentally. In contrast, the thermal imaging data of Lum et al. [41] and Matson [42] show that the envelope of the solid-liquid interface becomes spherical for $\Delta T > \Delta T_c$ as opposed to angular for $\Delta T < \Delta T_c$, which suggests that dendrites cease to exist for $\Delta T > \Delta T_c$ in apparent disagreement with the present results.

Phase-field simulations in which the anisotropy parameters are systematically varied show that the growth rate and morphology depend sensitively on the kinetic anisotropy. In particular, they show that dendrites cease to exist above a critical undercooling comparable to ΔT_c if the kinetic anisotropy is about one order of magnitude smaller than presently estimated by the atomistic simulations. For $\Delta T > \Delta T_c$, these simulations yield a dense-branching morphology characteristic of tip-splitting-dominated growth. Furthermore, they show that the doublon (triplet) in 2-d (3-d) does not appear to be the underlying building block of this morphology in this strongly kinetic-dominated regime, in contrast to the seaweed structure that has been simulated in 2-d without kinetics [51] or with the much smaller value of β_0 based on the Turnbull model (and noise) [54].

The phase-field results are in good quantitative agreement with the predictions of a linearized solvability theory that includes both capillary and kinetic effects [50]. This theory predicts dendrite velocities that are in remarkably good quantitative agreement with phase-field results for the large kinetic anisotropy value predicted by the MD simulations. Furthermore, it predicts that for a weak kinetic anisotropy, the steady-state dendrite branch terminates at some critical undercooling by merging with a lower velocity unstable branch. This provides a natural explanation for the disappearance of dendrites in the phase-field simulations with a sufficiently weak kinetic anisotropy, even without noise.

These results emphasize the need for a precise knowledge of both the magnitude of the kinetic coefficient (β_0) and its anisotropy (ϵ_k) to model reliably morphological evolution in a kinetic-dominated growth regime. There is still a significant uncertainty in the value of ϵ_k obtained by MD simulations [31]. The present simulations, however, do show that ϵ_k must be large, as predicted [31], to reasonably fit the dendrite velocity data for $\Delta T < \Delta T_c$. This is, of course, if one uses the value of β_0 predicted by both MD simulations and the BGK model [35], which is much less uncertain than the anisotropy.

We are led to conclude that, if the present anisotropy value is confirmed, the widely observed velocity break in the $V - \Delta T$ curve [38–42] is not reproduced by the standard model of the solidification of a pure melt with purely diffusive transport. This suggests that this break, and the associated envelope transition [42], may be caused by flow effects or dilute impurities. The latter seems possible since even very dilute impurities in Cu have been shown to influence the dendrite velocity and grain structure [58]. An extension of the present study to link atomistic and phase-field simulations in alloys is currently in progress to test this hypothesis and its consequences for grain refinement [60].

Acknowledgments

This research was supported by the US Department of Energy through grant No. DE-FG02-92ER45471 and additional funds provided by the Computational Materials Science Network. Computations were carried out at NERSC and NU-ASCC. We wish to thank Jeff Hoyt and Mark Asta for valuable discussions and input.

References

1. R. Trivedi and A. Karma, Encyclopedia of Applied Physics **23**, 441 (1998).
2. W. Kurz and D.J. Fisher, *Fundamentals of Solidification* (Trans Tech, Switzerland, 1989).
3. D. Kessler, J. Koplik, and H. Levine, Adv. Phys. **37**, 255 (1988).
4. J.S. Langer, in *Chance and Matter*, Lectures on the Theory of Pattern Formation, Les Houches, Session XLVI, edited by J. Souletie, J. Vannimenus, and R. Stora (North Holland, Amsterdam, 1987), p. 629.
5. A. Karma, in *Branching in Nature*, Lectures on Dendritic Growth, Les Houches, edited by V. Fleury, J.F. Gouyet, and M. Lonetti (EDP Sciences/Springer-Verlag, 2001), Vol. 13, Ch. XI, p. 365.
6. G.P. Ivantsov, Dokl. Akad. Nauk SSSR **58**, 567 (1947).
7. M.E. Glicksman, R.J. Schaefer, and J.D. Ayers, Metall. Trans. A **7**, 1747 (1976).
8. D.A. Kessler, J. Koplik, and H. Levine, Phys. Rev. A **31**, 1712 (1985).
9. E. Ben-Jacob, N.D. Goldenfeld, B.G. Kotliar, and J.S. Langer, Phys. Rev. Lett. **53**, 2110 (1984).
10. J.S. Langer, Phys. Rev. A **33**, 435 (1986).
11. D.A. Kessler and H. Levine, Phys. Rev. B **33**, 7687 (1986).
12. D.I. Meiron, Phys. Rev. A **33**, 2704 (1986).
13. M. Ben Amar and B. Moussallam, Physica D **25**, 155 (1987).
14. A. Barbieri and J.S. Langer, Phys. Rev. A **39**, 5314 (1989).
15. D.A. Kessler and H. Levine, Acta Metall. **36**, 2693 (1988).
16. M. Ben Amar and E. Brener, Phys. Rev. Lett. **71**, 589 (1993).
17. D.A. Kessler and H. Levine, Phys. Rev. Lett. **57**, 3069 (1986).
18. J.B. Collins and H. Levine, Phys. Rev. B **31**, 6119 (1985); J.S. Langer, in *Directions in Condensed Matter*, edited by G. Grinstein and G. Mazenko (World Scientific, Singapore, 1986), p. 164; G. Caginalp and P. Fife, Phys. Rev. B **33**, 7792 (1986).
19. R. Kobayashi, Physica D **63**, 410 (1993).
20. J.A. Warren and W.J. Boettinger, Acta Metall. Mater. A **43**, 689 (1995).
21. S.-L. Wang and R.F. Sekerka, Phys. Rev. E **53**, 3760 (1996).
22. A. Karma and W.J. Rappel, Phys. Rev. E **53**, R3017 (1996); Phys. Rev. E **57**, 4323 (1998).
23. N. Provatas, N. Goldenfeld, and J. Dantzig, Phys. Rev. Lett. **80**, 3308 (1998).
24. Y.-T. Kim, N. Provatas, N. Goldenfeld, and J.A. Dantzig, Phys. Rev. E **59**, 2549 (1999).
25. A. Karma and W.-J. Rappel, Phys. Rev. E **60**, 3614 (1999).
26. M. Plapp and A. Karma, Phys. Rev. Lett. **84**, 1740 (2000); J. Comp. Phys. **165**, 592 (2000).
27. S.-C. Huang and M.E. Glicksman, Acta Metall. **29**, 701 (1981).
28. M.E. Glicksman and N.B. Singh, J. Cryst. Growth **98**, 277 (1989).
29. M. Muschol, D. Liu, and H.Z. Cummins, Phys. Rev. A **46**, 1038 (1992).
30. R. Trivedi, Interface Science (current issue).
31. J.J. Hoyt, B. Sadigh, M. Asta, and S.M. Foiles, Acta Mater. **47**, 3181 (1999).
32. J.J. Hoyt, M. Asta, and A. Karma, Phys. Rev. Lett. **86**, 5530 (2001).
33. J.R. Morris, Z.Y. Lu, and K.M. Ho, Interface Science (current issue).
34. H. Ramalingam, M. Asta, A. van de Walle, and J.J. Hoyt, Interface Science (current issue).
35. J.Q. Broughton, G.H. Gilmer, and K.A. Jackson, Phys. Rev. Lett. **49**, 1496 (1982).
36. D. Turnbull, Metall. Trans. A **12**, 695 (1981).
37. H.E. Huitema, M.J. Vlot, and J.P. van der Eerden, J. Chem Phys. **111**, 4714 (1999).
38. J.W. Walker, in *Principles of Solidification*, edited by B. Chalmers (John Wiley and Sons, New York, 1964), p. 114.
39. R. Willnecker, D.M. Herlach, and B. Feuerbacher, Phys. Rev. Lett. **62**, 2707 (1989).
40. W.H. Hofmeister, R.J. Bayuzick, and M.B. Robinson, Rev. Sci. Instrum. **61**, 2220 (1990).
41. J.W. Lum, D.M. Matson, and M.C. Flemings, Metall. Mater. Trans. B **27**, 865 (1996).
42. D.M. Matson, in Solidification 1998, edited by S.P. Marsh, J.A. Dantzig, R. Trivedi, W. Hofmeister, M.G. Chu, E.J. Lavernia, and J.-H. Chun (The Mineral, Metals and Materials Society, 1998), p. 233.
43. G. Caginalp and X. Chen, in *On the Evolution of Phase Boundaries*, edited by M.E. Gurtin and G.B. McFadden, The IMA Volumes in Mathematics and Its Applications (Springer-Verlag, New York, 1992), Vol. 43, p. 1.
44. B.I. Halperin, P.C. Hohenberg, and S.-K. Ma, Phys. Rev. B **10**, 139 (1974).
45. K.R. Elder, F. Drolet, J.M. Kosterlitz, and M. Grant, Phys. Rev. Lett. **72**, 677 (1994).
46. S.G. Pavlik and R.F. Sekerka, Physica A **268**, 283 (1999).
47. J.J. Hoyt (private communication).
48. E. Ben-Jacob, G. Deutscher, P. Garik, N. Goldenfeld, and Y. Lareah, Phys. Rev. Lett. **57**, 1903 (1986).
49. Y.H. Lee, Ph.D. Thesis, Northeastern University, 1998.
50. Y.H. Lee, J. Bragard, and A. Karma (to be published).
51. E. Brener, H. Müller-Krumbhaar, and D. Temkin, Phys. Rev. E **54**, 2714 (1996).
52. T. Abel, E. Brener, and H. Müller-Krumbhaar, Phys. Rev. E **55**, 7789 (1997).
53. A. Karma, Y.H. Lee, and M. Plapp, in Proceedings of the M.C. Flemings Symposium on Solidification and Materials Processing, edited by R. Abbaschian, H. Brody, and A. Mortensen (The Mineral, Metals and Materials Society, 2001), p. 113.
54. A.M. Mullis and R.F. Cochrane, Acta Mater. **49**, 2205 (2001).
55. M. Ben Amar, Phys. Rev. A **41**, 2080 (1990).
56. G. Horvay, Int. J. Heat Mass. Transfer **8**, 195 (1965).
57. J.L. Walker, in *Physical Chemistry of Process Metallurgy* (John Willey, New York, 1956).
58. R.F. Cochrane, S.E. Battersby, and A.M. Mullis, in *Solidification 1998*, edited by S.P. Marsh, J.A. Dantzig, R. Trivedi, W. Hofmeister, M.G. Chu, E.J. Lavernia, and J.-H. Chun (The Mineral, Metals and Materials Society, 1998), p. 223.
59. M.J. Aziz, J. Appl. Phys. **53**, 1158 (1982).
60. A. Karma, Int. J. Non-Equil. Process. **11**, 201 (1998).